



Final Draft **of the original manuscript**

Tie, D.; Liu, H.; Guan, R.; Holt-Torres, P.; Liu, Y.; Wang, Y.; Hort, N.:
**In vivo assessment of biodegradable magnesium alloy
ureteral stents in a pig model.**

In: Acta Biomaterialia. Vol. 116 (2020) 415 - 425.

First published online by Elsevier: 16.09.2020

<https://dx.doi.org/10.1016/j.actbio.2020.09.023>

In vivo Assessment of Biodegradable Magnesium Alloy Ureteral Stents in a Pig Model

Di Tie ^a, Huinan Liu ^{b,c}, Renguo Guan ^{a,*}, Patricia Holt-Torres ^{b,c}, Yili Liu ^d,
Yang Wang ^e, Norbert Hort ^{f,*}

^a *School of Materials Science and Engineering, Northeastern University, Shenyang 110819, China*

^b *Department of Bioengineering, Bourns College of Engineering, University of California at Riverside, CA 92521, USA.*

^c *Microbiology Program, University of California at Riverside, CA 92521, USA*

^d *Department of Urology, China Medical University, Shenyang 110084, China*

^e *Animal Experimental Center, General Hospital of Northern Theater Command, Shenyang 110045, China*

^f *Magnesium Innovation Center, Helmholtz-Zentrum Geesthacht, D-21502 Geesthacht, Germany*

* Corresponding authors, E-mail addresses:

guanrenguo@126.com (Renguo Guan)

norbert.hort@hzg.de (Norbert Hort)

Abstract

Today, ureteral stent technology is making progress towards the reduction of complications and patient discomfort. Therefore, magnesium alloys have become excellent candidate materials for manufacturing ureteral stents due to their biodegradability and antibacterial activity. Built on our previous work on biodegradable magnesium alloys, this article reports a semisolid rheo-formed magnesium implant that displays degradability and biocompatibility *in vivo*, and feasibility as ureteral stents in a pig model. Refined non-dendritic microstructure was observed in the rheo-formed alloy, whose grain size and shape factor were ca. 25.2 μm and ca. 1.56 respectively. Neither post-interventional inflammation nor pathological changes were observed in the urinary system during the implantation period of 14 weeks, and the degradation profile (14 weeks) meets the common requirement for the indwelling time of ureteral stents (8 to 16 weeks). Furthermore, histopathological observation and urinalysis results confirmed that the alloy had significantly higher antibacterial activity than the medical-grade stainless steel control. To our knowledge, this is the first *in vivo* study of biodegradable magnesium alloy as urinary implants in large animal models. Our results demonstrate that magnesium alloys may be a reasonable option for manufacturing biodegradable ureteral stents.

Keywords

In vivo; Magnesium alloy; Ureteral stent; Biodegradable; Biocompatibility.

Introduction

In the 1850s, Dr. Charles Thomas Stent invented the first stent to take impressions of teeth, and after whom the stent was named [1, 2]. After that “stenting” became the term to describe this type of surgery, which was eventually used in other anatomical locations such as placing a supporting device in the urinary tract to facilitate urine flow [2, 3]. Stenting was first introduced in urology in the 1970s, when Goodwin wrote a brief letter, *Splint, Stent, Stint* [4]. After that, ureteral stents were widely used in urinary-tract operations [2-4]. Silicone and polyurethane became the materials of choice in the early stages of stent development because they could reduce encrustation [1]. Later, the modern Double-J Stents (DJs) developed by Roy Finney and Thomas Hepperlen were widely used in the urinary tract [5]. The objective of this most recent stent study has made steps towards meeting clinical demands, including reduction of complications, convenience of extraction, and less patient discomfort [6]. After serving their function in the body, ureteral stents can be removed by cystoscopic procedures under general anesthesia [7]. However, the procedures for ureteral stent removal often causes physical discomfort and poses additional economic burdens for both the patients and healthcare system. Moreover, repeated exposure to anesthesia is undesirable [8-10]. Therefore, alternative stenting devices that can effectively drain urine while eliminating the secondary surgeries for stent removal are actively pursued [11, 12].

An ideal material for manufacturing ureteral stents should be fully degradable *in vivo*. Biodegradable materials, also known as bioabsorbable materials, can degrade gradually in human body without inducing cytotoxicity [13, 14]. Several studies have reported the use of biodegradable polymers for urinary stents. For example, Soria *et al.* [11] reported a biodegradable polymer based urinary stent composed of Glycomer 631 and polyglycolic acid, and the tensile strength of this polymer stent was 57 MPa. Barros *et al.* [15] developed a biodegradable gelatin-based drug-eluting ureteral stent for the treatment of upper tract carcinoma, and the mechanical properties were reported to be lower than commonly used polymer materials. In contrast to polymer-based biodegradable urinary stents, metallic biodegradable stents have attracted significant attention more recently, because mechanical properties of metals are inherently better than polymers and are more desirable for stent dilatation.

Application of biodegradable metals in urology is an innovative concept first reported by Lock *et al* [16]. Specifically, our study on degradability and antibacterial activity of pure magnesium, Mg-Y alloys and AZ31 alloy in artificial urine first demonstrated the potential of biodegradable magnesium alloys for urological applications [12, 16]. Up to now, very few studies have reported on the use of biodegradable metallic ureteral stents. In 2017, Zhang *et al.* [17] demonstrated that pure magnesium, Mg-6Zn (mass%) alloy and ZK60 alloy have no significant adverse effects on rat bladders and no significant toxicity towards rat livers and kidneys. A more recent study by Champagne *et al.* [12] revealed slower *in vitro* corrosion rates of pure zinc and zinc alloys (Zn-0.5mass%Mg, Zn-1mass%Mg and Zn-0.5mass%Al)

than pure magnesium and a Mg-Zn-Mn alloy. However, considering that the average clinical indwelling time of ureteral stents is 8 to 12 weeks, magnesium alloys exhibited the closest degradation period that matches the clinical need [18, 19]. Iron and zinc, as another two widely studied biodegradable metals, usually have much longer degradation time than magnesium and its alloys according to Bowen *et al.* [20] and Hernandez-Escobar *et al.* [21]. The antibacterial activity of magnesium alloys when used as ureteral implant materials is another advantage [22, 23]. Therefore, when compared with other potential biodegradable metallic materials, such as iron and zinc, magnesium is a better candidate for manufacturing ureteral stents due to its suitable corrosion rate and antimicrobial activities against a wide range of bacteria and yeasts that are found in clinical infections.

This is the first *in vivo* study in a large animal model to evaluate the feasibility of ureteral stents made of magnesium alloys. In our previous studies, we developed a Mg-Ag alloy series as biodegradable and antibacterial materials [24], and biodegradable Mg-Sr alloys for bone fracture fixation [25]. We also investigated the cytotoxicity of Mg-4Zn-1Sr (mass%, ZJ41) with human urothelial cells and their degradation behavior *in vitro* [26]. Built on our previous results, the objectives of this study were to fabricate ZJ41 alloy based ureteral stents, characterize their microstructure and electrochemical properties, evaluate their *in vitro* cytotoxicity, investigate the *in vivo* degradability, histocompatibility, and biocompatibility of ZJ41 alloy based ureteral stents in a large animal model, and determine the feasibility of ZJ41 alloy for urological implant applications and clinical translation. To simulate the

stent implantation in a human body, *Guangxi Bama Minipig* was selected as an ideal animal model for this *in vivo* study [27]. From application perspective, Mg-based ureteral stents are more desirable to replace current permanent metal stents for a longer dwelling time rather than short-term usage. Thus, we chose stainless steel as the control material, because other ureteral implant materials represented by polymers are intended for shorter dwelling time. In this study, a unique semisolid rheo-forming process was used for manufacturing the Mg alloy based ureteral stents [28].

Rheo-forming process can produce refined non-dendritic microstructures and lead to significant differences in mechanical strength between primary solid phases and secondary phases [29]. As a result, the microstructure and mechanical properties of rheo-formed magnesium alloys are superior when compared with the magnesium alloys solidified using traditional metallurgical processing [30]. This study provides critical results for demonstrating ZJ41 magnesium alloy as a potential alternative for manufacturing biodegradable ureteral stents.

2. Materials and methods

2.1. Material preparation

The alloy material used for this study is ZJ41 and is named according to American Society for Testing and Materials' guidelines. ZJ41 alloy has a nominal composition of 4.00 mass% Zn and 1.00 mass% Sr in a Mg matrix. Pure zinc (99.99 mass%, Zhuye Group, Zhuzhou, China) and Mg-10Sr (mass%) alloy (Norsk Hydro A.

S., Oslo, Norway) was mixed with pure Mg (99.999 mass%; Luxfer, Manchester, UK) and melted according to the nominal composition at 720.0 °C under a protective atmosphere (pure argon + 2.0 vol.% SF₆) in a resistance furnace (Hengli HLJ, Henan, China). The semisolid slurry was prepared by a rheological pulping system utilizing a vibration device designed by ourselves (Fig. 1a; [28]). The melting temperature was ca. 685.0 °C, and within the semisolid temperature range for this alloy. The prepared melt was transferred into a continuous rheo-extrusion machine to produce alloy wire with a diameter of 1.0 mm [28]. The alloy wire was then made into stents using a manual coiler, whose size is depicted in Fig. 1a.

2.2. Material characterization and corrosion tests

An inductively coupled plasma optical emission spectrometer (ICP-OES; Varian, USA) was employed for the analysis of the actual chemical composition of the ZJ41 alloy. A tension test was performed using tensile testing (Z050, Zwick, Ulm, Germany). Specimens were collected from the cross section of the stent for microstructural characterization after mechanical polishing with SiC paper and mechanical polishing slurry (Yuanshimoju, Chengdu, China). A visible light microscope (DSX-500, Olympus, Japan) was employed to characterize the optical microstructure of the alloy in more precise scale. The surface elemental distributions were analyzed using scanning electron microscopy (SEM, Ultra Plus, Carl-Zeiss, UK) equipped with an energy dispersive X-ray spectrometer (EDS; Ametek, New Jersey, USA). The phase identification was conducted by X-ray diffraction analysis (XRD, Siemens, München, Germany). The step time was set at 3.00 s and the step size was

20.0 μm . A high-resolution transmission electron microscope (HR-TEM; Tecnai, FEI, Eindhoven, Netherlands) was also utilized for a more accurate phase identification.

Single sweep voltammetry, cyclic voltammetry and electrochemical impedance spectroscopy (EIS) was performed to evaluate the corrosion properties of the alloy using an electrochemical workstation (Parstat, Princeton, USA). The reference electrode used was a saturated calomel electrode (SHE) and the test potential range was from -1.60 V (vs. SHE) to -0.70 V (vs. SHE) for linear sweep voltammetry testing. The open circuit potential (OCP) was measured and the cyclic voltammetry test was carried out from -0.50 V (vs. OCP) to +0.50 V (vs. OCP). The surface status was further analyzed by electrochemical impedance spectroscopy (EIS) analysis between 0.10 mHz and 0.01 Hz by a sinusoidal potential of 5.0 mV at OCP. Artificial urine (AU) was prepared according to our previous study and used as the corrosion media. All the experiments were performed under cell culture conditions (37.0 °C, 20.0 vol.% O₂, 5.0 vol.% CO₂, 95.0% relative humidity).

After evaluating the material's corrosion properties via electrochemical tests, the stents were tested by immersion in AU (10 mL) to determine the ion release and their *in vitro* corrosion rate. The specimens were incubated under cell culture conditions for up to 14 days. The pH value of the extract was determined every 2 days by use of a pH meter (PH210, Hanna, Woonsocket, USA). The surface products were removed by rinsing with chromic acid solution (200 g·L⁻¹) for mass determination. The average

corrosion rate (CR) of the test stents were expressed as millimeters per year ($\text{mm}\cdot\text{y}^{-1}$) [25].

2.3. *In vitro* cytocompatibility and cell proliferation

Human normal liver cells (LO2) were provided by Shanghai Cell Bank of Chinese Academy of Sciences and cultured in DMEM with 15 vol.% FBS. To evaluate the cytocompatibility of the ZJ41 alloy, a widely used metallic material in the urinary system, 316L medical stainless steel (SS), was also tested as a reference, and with cell-culture treated well-plates as the control group. The seeding density was 1×10^4 cells mL^{-1} and the incubation period was 21 days. Fluorescence microscopy (Eclipse, Nikon, Shanghai, China) was employed to observe the cellular morphology. Cell proliferation was characterized with a Cell Counting Kit (CCK-8; Meilunbio, Dalian, China) and the fluorescence of treated LO2 cells was collected using a microplate reader (Thermo Fisher, Waltham, USA) at a wavelength of 450 nm.

2.4. Animals and surgical procedures

The size of implanted stents and the surgical procedure used are shown in Fig. 1A. All animal procedures were approved by our local animal welfare committee (DB11/T 1463.1-2017) and conducted according to the guidelines issued by the State Scientific and Technological Commission, China [31]. *Guangxi Bama Minipigs* were chosen for this study as they are an ideal large animal model for *in vivo* experiments [27]. Eight-week old females (Northern Theater General Hospital, Shenyang, China) were divided into three groups: ZJ41 group ($n = 3$), SS group ($n = 3$) and blank control

group (n = 3), and raised for 14 weeks within sterile cages at 25 °C. Adequate food and drinking water (Shenyang Agricultural University, Liaoning, China) was supplied without restrictions to the animals.

2.5. *In vivo* degradation behavior

Positron emission tomography computed tomography scanner (PET-CT; Discovery VCT, GE, Boston, USA) was employed at 0, 7, and 14 weeks post-implantation to examine the degradation of implant materials with corresponding post-interventional inflammation or pathological changes in the urinary systems of the animals. The residual mass of the stent was calculated by the total urine magnesium content using a magnesium ion selective electrode (DX224, Mettler Toledo, Zurich, Switzerland). Stents were removed at 7 weeks and 14 weeks post-implantation and the surface morphology was observed using SEM. X-ray induced photoelectron spectroscopy (XPS; Kratos, Manchester, UK) analysis and Casa software (Casa Soft, Teighnmouth, UK) were used to identify the composition of the surface magnesium corrosion products.

2.6. *In vivo* biocompatibility

At 14 weeks post implantation, myocardium and liver lobules were harvested from the animals. The tissues were sectioned and H/E (hematoxylin and eosin) stained for histological examination [32]. A biomicroscope (X71, Olympus, Tokyo, Japan) was employed for histopathological observation. Liver function of the test animals was assessed every 4 weeks through the measurement of serum concentrations for

total bile acid (TBA), total bilirubin levels (TBIL), aspartate aminotransferase (AST) and alanine aminotransferase (ALT). These four indices can sensitively represent liver function because impaired liver function will lead to a rapid upregulation of these indices [33]. Furthermore, cardiac function markers including serum lactate dehydrogenase (LDH), creatine phosphokinase (CK) and α -hydroxybutyrate dehydrogenase (α -HBDH) were assessed every 4 weeks also. These highly specific markers are widely utilized as cardiac damage indicators because their concentration will immediately increase in blood serum when cardiac damage occurs [34].

Hematology analyses were completed using blood samples collected every 7 weeks using a Biochemical Autoanalyzer (Type 7170, Hitachi, Tokyo, Japan), and important hematology markers were measured: blood glucose (Glu), red blood cell count, white blood cell count, hemoglobin and hematocrit. In addition,, serum albumin concentrations were also detected as an inflammation marker due to its sensitive downregulation during a host inflammatory response [35].

2.7. Impact on lower urinary tract and urination

2.7.1. Optical microscopic and transmission electron microscopic observation

At 14 weeks post implantation, the ureteral wall surrounding each implantation site was harvested from the animals. The tissue was then sectioned and H/E stained for histological examination. A biomicroscope (X71, Olympus, Tokyo, Japan) was employed for optical microscopic observation of these samples. To identify the potential degenerative changes and the alteration in cellular morphology, transmission

electron microscopy (TEM; JEM-2100F, Jeol Ltd, Mitaka, Japan) was employed. The transitional epithelium (ca. 1.0 mm³) was fixed in 2.50 vol.% glutaraldehyde solution for 3 hours. The specimens were dehydrated and embedded in epoxy resin in capsules and polymerized for 24 h at 60 °C. After embedding, the sections were micro-sliced by an ultra-microtome (SM2010, Leica Biosystems, Shanghai, China) and the sections examined.

2.7.2. Urination and urinalysis

To determine the urinary frequency of each test animal, chromatography filter paper (GE-Whatman, Kent, GB) placed under culture cages in two-hour increments. Each paper was vacuum dried and imaged using a UV-visible-NIR microscope (MJT Tech, Beijing, China) to determine the morphology of void spots. Following this, the spots were analyzed using ImageJ software (V1.5, Bharti Airtel Ltd., New Delhi, India) to calculate the urinary frequency. Midstream urine from all animals was investigated microbiologically every two weeks to evaluate the impact of implantation on urine and potential peri-implant infection. A urinalysis was performed using an automatic urine analyzer (iRicell, Beckman Coulter, Atlanta, USA) that determined the pH value, urinary white cell count, and urinary red cell count. Bacteriuria was tested via a standard quantitative urine culture method. Here, nonselective chromogenic agar plates (Forthright Biotech, Shanghai, China) were used as a quantitative reference while selective colistin-nalidixic acid agar plates (Forthright Biotech, Shanghai, China) enabled the identification of Gram-positive bacteria. The

plates were incubated at 35.0 °C for 24 hours before examination and the results were measured in the number of colony forming units (CFU ml⁻¹).

2.8. Statistical analysis

In vitro tests were performed with six duplicates for each *in vivo* group (ZJ41, SS and control) and each group was composed of three animals. Results were presented as mean value ± standard deviation (SD), and one-way analysis of variance test using SPSS V19.0 (SPSS Inc., Chicago, USA) was applied for comparisons of the means between different groups with confidence intervals of 95.0% (* $P < 0.05$), 99.0% (** $P < 0.01$) and 99.9% (***) $P < 0.001$). NS stands for no significant difference.

3. Results and discussion

3.1. Material characterization and *in vitro* assessment

The ZJ41 alloy was composed of a primary α -Mg solid phase and Zinc rich secondary phase due to the dynamical non-equilibrium solidification process. The grains were primarily equiaxed and spherical with the average size of 25.2 μm (Fig. 1b). The actual measured chemical composition of the ZJ41 alloy was Zn 4.11 ± 0.03 mass%, Sr 1.02 ± 0.01 mass% and balanced Mg. Impurities included Fe (< 0.01 mass%), Ni (< 0.01 mass%) and Cu (< 0.01 mass %). The ultimate tensile strength and the elongation of the rheo-formed ZJ41 alloy was 305.7 ± 4.2 MPa and $14.2\% \pm 0.3\%$, respectively. According to the SEM micrographs and the EDS maps (Fig. 1c, 1d), it is evident that both the eutectic structure and the small-sized Sr rich precipitates were generated during the semisolid extrusion process [28]. The precipitates distributed along grain boundaries were identified by EDS and XRD analysis (Fig. 1c, 1e), and were primarily composed of MgZn_2 and $\text{Mg}_{17}\text{Sr}_2$. The HR-TEM micrograph of the interface between the primary solid phase and the secondary grain phase with corresponding diffraction patterns of the precipitates in primary solid phase are represented in Fig. 1f. The diffraction pattern of the $\text{Mg}_{17}\text{Sr}_2$ phase can be indexed as metastable phases with base-centered orthorhombic structure, which had an equivalent diameter of ca. 4.0 nm and was predominantly dispersed inside primary solid phases (Fig. 1f) [25, 36].

In the later period of semisolid rheo-solidification, the temperature dropped to the eutectic temperature and led to eutectic reaction and non-equilibrium solidification [28]. During this process, the second phases precipitated at grain boundaries and formed a divorced eutectic structure (Fig. 1c). $\text{Mg}_{17}\text{Sr}_2$ has a body-centered cubic structure while MgZn_2 has a hexagonal structure [37]. The SEM micrographs and EDS maps showed most $\text{Mg}_{17}\text{Sr}_2$ phases precipitated together with MgZn_2 eutectic phases, indicating that the eutectic phases provided heterogeneous nucleation points during the precipitation process of $\text{Mg}_{17}\text{Sr}_2$. Therefore, the majority of the precipitates concentrated in secondary grain phases and bore shear stress during the rheo-solidification process. Sharp strength differences between primary solid phases and secondary grain phases further improved the effectiveness of semisolid slurring. As a result, a refined non-dendritic microstructure was observed in the rheo-extruded ZJ41 alloy, whose grain size and shape factor were only ca. 25.2 μm and ca. 1.56 respectively. The grain size and aspect ratio of the rheo-extruded ZJ41 alloy were much better than most Mg-Zn alloys solidified in traditional methods, leading to superior properties [30].

In the single sweep voltammogram of ZJ41 alloy (Fig. 2a), a shift of break down potential in the anodic direction near -1.04 V (*vs.* SHE) can be observed due to oxidation state changes. Alloying of zinc and strontium caused a lower slope of the anodic part of the curve compared to pure magnesium and also changed the pitting corrosion potential to the positive direction, hinting that both homogeneous and pitting corrosion were inhibited [38]. The cyclic voltammograms (Fig. 2b) show that the ZJ41

alloy had no hysteresis behavior, which indicates that no pitting corrosion occurred. The EIS results are presented in Nyquist diagram (Fig. 2c). At the initial phase, the inductive loop was attributed to ion release, while the diameter increase of the capacitive arc was ascribed to a thickened corrosion layer [39, 40]. The equivalent circuit was fitted by using M. Orazem *et al.*'s model as applied for the characterization of the interfacial processes (Fig. 2c) [41]. The pH value changes and the average corrosion rate changes of the samples calculated by mass loss are shown in Fig. 2d. The pH value varied within a narrow range from 6.45 to 6.95, and this stable pH environment was crucial for the validation of credible corrosion rate data. The highest corrosion rate ($0.63 \pm 0.02 \text{ mm}\cdot\text{y}^{-1}$) was observed within 2 days immersion time. With increasing immersion time, ZJ41 alloy exhibited a constantly decreasing corrosion rate of $0.31 \pm 0.02 \text{ mm}\cdot\text{y}^{-1}$ by the 14th day. Electron transportation was blocked due to the gradually thickening corrosion layer, and therefore the corrosion rate was significantly decreased [42].

The results for human hepatocyte viability after 7 days, 14 days, and 21 days culturing with tested materials are presented in Fig. 2e. These images display the fluorescence of hepatocyte cells attachment on the surface of SS and ZJ41 alloy. The CCK-8 assays also revealed that the cell proliferation rate of LO2 cells in the ZJ41 alloy group ($750.7\% \pm 43.2\%$) was not significantly ($P > 0.05$) different from SS group ($710.7\% \pm 56.1\%$) after 21 days culturing (Fig. 2e). The cell adhesion and proliferation results demonstrated that ZJ41 alloy has an equivalent level of cytocompatibility with medical stainless steel, which has been widely applied as a

non-toxic material in urinary systems [43]. These results also confirmed our previous study on the comparison of cytocompatibility among magnesium alloys (including ZJ41), titanium, polyurethane, and glass [26].

3.2. *In vivo* degradation and biocompatibility

Six animals in each test group underwent uneventful operative procedures and all nine animals (including three individuals in the control group) survived until the predetermined end point of 14 weeks. PET-CT was performed at 0 weeks, 7 weeks, and 14 weeks post-implantation. Although PET-CT is one of the most sensitive molecular imaging techniques, its resolution still did not allow for a precise observation of the implant degradation progress [44]. Therefore, we used PET-CT to determine the integrity of the ZJ41 implants as well as inflammatory changes at the implantation site (Fig. 3a) [45]. Neither post-interventional inflammation nor pathological changes in the urinary tract system were observed by PET-CT examination. The ZJ41 alloy stent still maintained its shape integrity after 7 weeks implantation, while the degradation process finished no later than 14 weeks post-implantation (Fig. 3a).

The normal urine magnesium content in the control group was 0.552 ± 0.008 $\text{mmol}\cdot\text{L}^{-1}$, in comparison to the calculated residual mass of the stents in the test group. The residual mass of the ZJ41 alloy decreased from 0.402 ± 0.002 g at 0 weeks to 0.113 ± 0.003 g at 7 weeks and was fully degraded at 12 weeks. The corrosion rate did

not fluctuate sharply during the implantation period. This indicated that structural failure did not occur as a result of the rheo-solidified microstructure (Fig. 3b) [46]. The avoidance of structural failures from high corrosion rates is crucial because corrosion failure is the primary limitation of Mg alloys applied as biodegradable implant materials [47]. It was also noted that the calculated peak corrosion rate *in vivo* was $4.68 \pm 0.06 \text{ mm}\cdot\text{y}^{-1}$, which was far higher than the *in vitro* value ($0.63 \pm 0.02 \text{ mm}\cdot\text{y}^{-1}$; Fig. 2d). Previously, it has been reported that flow-induced shear stress could accelerate the general corrosion as a result of increased mass transfer in the electrical double layer [48]. Our results are in agreement with these findings and confirm that urine flow might alter the degradation behavior of the ZJ41 alloy, especially when the stent is in direct contact with urine during the initial stage. Although the test stent showed an appropriate *in vivo* degradation period according to regular ureteral stent indwelling time (8 to 16 weeks), further *in situ* studies on its degradation behavior together with urodynamics analysis are still important in the future to optimize its structure and performance [18].

The principal difference between semisolid solidification and liquid solidification is the presence of rounded primary solid grains of α -phase solidified during the first stage of the solidification process [49]. The surface morphology of the ZJ41 stent after 7 weeks implantation also corresponded to the microstructure of the alloy before implantation (Fig. 3c). The secondary solid phases enriched with zinc and strontium had a more positive corrosion potential than the primary solid phases, and therefore formed a network-like cathode in galvanic corrosion [46, 49]. The cathodic network separated anodic areas composed by primary phases, and prevented corrosion products from spreading to other anodic areas. As a result, the alloy degraded through a general

corrosion process rather than localized corrosion (Fig. 3c) [46]. To analyze the *in vivo* degradation behavior of the alloy, we carried out XPS analysis for the surface products of the ZJ41 stent. The Mg 2p spectra (Fig. 3d) distributed between 47.0 eV and 53.0 eV, within which the signal could be deconvoluted to the Mg-(OH) sub-peak at 49.4 eV, the Mg-O sub-peak at 50.2 eV, and the Mg-PO₄ sub-peak at 50.8 eV [25, 50]. MgO, Mg(OH)₂ and hydroxyapatite were the main degradation products in the corrosion layer according to XPS analysis, while small amounts of ZnCl₂ and SrCl₂ were also distributed in the corrosion layer.

We evaluated the selected histological sections of the liver and myocardium at 14 weeks post-implantation to assess the possible systemic toxicity induced by the stent, focusing on lesions, inflammation, and tissue damage (Fig. 4). Integrated cellular structures and an absence of necrotic tissue were observed in all tissue sections from both test and control groups. No inflammatory infiltrate was found in hepatocytes and hepatic portal areas, while occasional necrosis of single cells and sinusoidal widening could be observed in both control and test groups (Fig. 4a). The biochemical results for hepatic functions determination are also shown in Fig. 4b. Higher expressions of AST, ALT, TBIL and TBA in serum were observed in the test groups during the initial phase of implantation and recovered to normal levels thereafter. Specifically, the highest ALT/AST ratio was measured for the SS group at 8 weeks post-implantation (1.88), which hinted at a transient fat metabolism disorder that may be the result of peri-implant infection [51]. Among liver function indices, the ALT/AST ratio is a powerful predictor of fat metabolism complications [52]. The ZJ41 group showed a similar ALT/AST ratio level with the control group, which could be attributed to

antibacterial activity of the degradation products [16, 51]. We will discuss the antibacterial activity of the ZJ41 alloy in more detail in the next section.

The nuclei and endomysium in the myocardium sections exhibited neither evident morphological changes nor hydropic degeneration (Fig. 4c). The results of cardiac function markers of test animals is presented in Fig. 4d. The results indicate that LDH significantly increased in both SS and ZJ41 groups at 4 weeks ($p < 0.001$) compared with the control group which is used as a main indicator of cardiac function [53]. The LDH serum concentration in the test groups rapidly returned to normal levels at 8 weeks, indicating recovery from surgery by test animals [54]. There were also significant differences in the serum concentrations of CK and α -HBDH at 4 weeks ($p < 0.001$), whereas their levels also returned to normal at 8 weeks in comparison with the control group ($70.3 \pm 8.1 \text{ U}\cdot\text{L}^{-1}$ and $81.0 \pm 3.5 \text{ U}\cdot\text{L}^{-1}$, respectively). Fig. 4e summarizes the results of inflammation and hematological analysis and showed no obvious adverse effects on physiological indicators in the ZJ41 group. It is worth noting that a significantly higher leukocyte level was found in the SS group versus the ZJ41 group at 7 weeks post-implantation ($p < 0.01$) which was a clear demonstration of severe peri-implant infection [55]. Given the ZJ41 stent had fully degraded at 12 weeks post-implantation, the main hematological and inflammation indices of animals in the ZJ41 group could return to normal levels more quickly than those in the SS group. From this point of view, the advantage of a degradable stent is not just immunity to a second operation, but also freedom from adverse effects brought about by extra indwelling time.

3.3. Impact on lower urinary tract and applicability evaluation

Evidence of calcification toward the luminal aspect of the ureter wall was identified in the SS group, where a peri-implant infection also occurred (Fig. 5a). There was neither loss of transitional epithelium nor von Brunn's nest in test groups, which suggested that severe epithelium lesions were not present. Thicker, newly formed muscularis at the implantation site was observed and is considered a normal variant found in upper urinary tract operations. On a cellular level, implantation induced neither degenerative changes nor enlargement of cell sizes (Fig. 5a). Light cytoplasm as well as compact chromatin were observed in transitional epithelium. With local Mg^{2+} ion supplies available in the ZJ41 group, we noted a decrease in widening of the lamina propria as well as an absence of nucleus fragmentation in comparison to the SS group. It is suspected that inhibitions to peri-implant infection effectively prevented these changes in ureter structure [56].

As has been observed previously in post-operative care, stent implantation negatively impacted bladder function. SS and ZJ41 stents significantly increased the frequency of urination during the first few weeks post-implantation (Fig. 5b). In addition, peri-implant infections increased the number of bacteria within the bladder and lead to a reduced bladder capacity and frequent small urination events, suggesting an increased sensation to urinate post-implantation [57]. Due to its decreasing volume and antibacterial activity, ZJ41 stents exhibited significantly ($P < 0.001$) less influence on urination (14.00 urination per day) compared to SS stents (25.33 urination per day) at 2 weeks post-implantation. Along with postoperative recovery, urinary frequency in test animals was reduced to a normal level after 6 weeks post-implantation. As shown in Fig. 5c, a sharp increase in the pH value of urine collected from the ZJ41 group

corresponded to the degradation of the alloy material. Interestingly, regardless of many previous reports on pH value change in *in vitro* studies, an increase in pH at implantation sites is scarcely reported. Notable urinalysis data also included elevated white blood cell counts (4.33 in SS and 2.66 in ZJ41 at 7 weeks post-implantation; 3.00 in SS and 0.66 in ZJ41 at 14 weeks post implantation), and elevated bacteria numbers (133 CFU·mL⁻¹ in SS and 105 CFU·mL⁻¹ in ZJ41 at 7 weeks post implantation; 101 CFU·mL⁻¹ in SS and 72 CFU·mL⁻¹ in ZJ41 at 14 weeks post-implantation). Both urinalysis and urine bacterial culture results indicated that peri-implant infections did occur, but recovery occurred during the 14 week implantation period, whereas no evidence of urinary tract obstruction was noted during urination monitoring (Fig. 5b). Urinalysis results confirmed significantly higher antibacterial activity by the ZJ41 than the SS stent. This agreed with the hematological and inflammation indices results.

The foremost advantages of a biodegradable ureteral stent include immunity to both a second operation and adverse effects brought about by extended indwelling time. After urological procedures, a temporary metallic Double-J ureteral stent (DJs), usually manufactured of medical stainless steel or titanium, is necessarily implanted in the ureter for optimal healing of the suture lines and drainage of the urinary system. After serving its purpose, the DJs are removed by cystoscope under anesthesia [7]. This additional exposure to anesthesia along with the financial burden of a secondary medical procedure, have become important disadvantages for the placement of ureteral stents in urological procedures [8-10]. Therefore, some investigators are seeking alternate implant materials either to drain the urinary system or to avoid a second

surgery to remove the implant. Soria *et al.* [11] reported a polymer-based biodegradable ureteral stent composed of Glycomer 631 and polyglycolic acid, whose tensile strength is ca. 57 MPa. Barros *et al.* [15] prepared a biodegradable ureteral stent for treatment of upper urinary tract carcinoma, which was composed of 65 mass% gelatin, 30 mass% alginic acid sodium salt and 5 mass% bismuth (III) carbonate and whose tensile strength is even lower than commonly used polymer materials. Compared to polymer-based biodegradable urinary stents, metallic biodegradable stents have inherent advantages that include similar mechanical properties to traditional DJJs. For example, the ZJ41 alloy used in our study could achieve an ultimate tensile strength of over 300 MPa after rheo-forming due to twins-stacking strengthening effects [58]. Compared to other potential biodegradable metallic materials, especially iron and zinc, magnesium is a better candidate for ureteral stents because its degradation rate is in the suitable range for clinical applications and can be adjusted. Given the average clinical stent indwelling time is 8 to 12 weeks, ZJ41 exhibited the closest matching degradation period (Fig. 3b) [18]. Iron and zinc are another two widely studied biodegradable metals, but they degrade much slower than magnesium, thus requiring longer periods for their degradation [20, 21].

The antibacterial activity of magnesium alloys when used as ureteral implant materials is another significant advantage. Ureteral stents represented by DJJs have become important integral parts of urological implant devices. However, complications such as urinary tract infections still emerge with long-term use of indwelling stents [59]. Alternative materials including polyurethane, polyethylene and

drug delivery materials have been developed to decrease the infection rates of ureteral stents [60]. However, management of biofilm-based infections remains problematic [61]. For example, systemic antibiotic therapy is one of the most common and effective methods to eliminate circulating bacteria, but this usually fails to protect the stent surface from bacterial colonization and leaves the patient at continuous risk of complications [61, 62]. To illustrate, Kehinde *et al.* [63] reported that the incidence of bacteriuria after DJs implantation was significantly increased with longer indwelling time. In comparison, the constantly degrading surface of magnesium alloys could inhibit bacterial adhesion because the antimicrobial degradation products could interrupt the stability of biofilms, potentially reducing the risk for complications over time [16, 64].

Different from permanent implant materials, biodegradable magnesium alloy has a constantly exfoliated surface, on which biofilm can hardly form [16]. Robinson *et al.* [65] reported that the increase of pH due to presence of Mg^{2+} significantly decreased the number of CFUs. Lellouch *et al.* [23] reported that MgF_2 nanoparticles could inhibit the growth of *E. coli* by attaching and penetrating its cellular membrane. We also observed significant decreased bacterial proliferation on the surfaces of pure magnesium and several magnesium alloys [16]. Both alkalinity and increased Mg^{2+} concentration during degradation contributed to inhibition of bacterial growth, and the corrosion products including magnesium hydroxide and magnesium oxide particles also contributed to bacteria death [66]. Although our results have proved significant antibacterial activity of ZJ41 alloy *in vivo* (Fig. 4 and 5), it is still essential to

comprehensively study the mechanism of magnesium alloys in the inhibition of biofilm formation and bacterial growth when translating magnesium alloys to clinical applications.

When attempting to reduce the adverse effects associated with ureteral stents, another crucial issue is the formation of ureteral obstructions [67, 68]. Among surgical complications that result from ureteral implantation operations, ureteral obstructions are primarily caused by ureteral stones that are present at an incidence rate of over 10% [68]. Baumgarten *et al.* [69] examined ureter passage rates of 119 patients after DJs implantation, and the average passage rate was 14%. In Kuebker *et al.*'s study [70], 8% of patients treated with a stent implantation experienced ureteral obstruction. In contrast to permanent metallic ureteral stents, magnesium ureteral stents are fully degradable. The ZJ41 stent tested in our study fully degraded at 12-week post-implantation (Fig. 3), and avoided the risk of ureteral obstruction induced by extra indwelling time. Furthermore, the antibacterial activity also plays an important role in the prevention of ureteral stones. Some bacterial species such as *Proteus* and *K. pneumoniae*, produce the enzyme urease which hydrolyses urea into ammonia and carbonic acid which can contribute to ureteral stone formation [71, 72]. Therefore, avoiding ureteral stones is important in the treatment of ureteral obstruction as ureteral stones can lead to urinary tract infections, and persistent infections can cause ongoing stone formation [73]. Hence, the significant antibacterial activity of ZJ41 alloy (Fig. 5c) could also be attributed to a reduction in the occurrence of ureteral stones after stenting. Previous studies on other potential biodegradable metals have advocated the

same. An iron-based biodegradable alloy was tested for antibacterial activity and was found to effectively kill bacteria and inhibit the formation of bacterial biofilms [74]. The antibacterial activity of this alloy primarily resulted from the Cu^{2+} that was released from the alloy surface during degradation. Similar with some well-known antibacterial metals including silver and copper, the antibacterial activity of magnesium alloys mainly relies on ion release and therefore has a broad antibacterial spectrum [64, 75, 76]. Compared to other biodegradable metallic materials, magnesium has another advantage in the reduction of ureteral stones because of its relatively short and adjustable indwelling time [13, 20, 21]. As we discussed in the last section, the degradation period of ZJ41 alloy is compatible with an effective treatment cycle, and thus the incidence of ureteral stones and other associated adverse effects could be further reduced.

In summary, biodegradable biocompatible ZJ41 magnesium alloys may be a new promising option for manufacturing ureteral stents. ZJ41 alloy can be further fine-tuned in the processing to have adjustable indwelling time for its applications in different stent types. Biodegradable ZJ41 magnesium alloy stents are especially desirable for the patients in poor physical condition, if avoiding secondary surgical procedures is a priority for them. The major limitation of the study is that this is a single center animal study with limited number of animals, which would require from additional data from other investigators. Future study will also focus on the direct comparison with other magnesium alloys and the treatment effects of long-term implantation.

4. Conclusions

We developed a biodegradable magnesium alloy ureteral stent and compared its performance with stainless steel in the porcine ureter models for 14 weeks. In contrast to the traditional alloy processing, the rheo-solidification process led to a more refined microstructure, higher tensile strength, and more homogeneous corrosion rate in the Mg alloys. The degradation period of our magnesium alloy stents perfectly matches the expected indwelling time of clinical ureteral stents, and our biodegradable alloy stents caused neither post-interventional inflammation nor pathological changes in the host urinary system. In comparison with the widely used ureteral stent material such as stainless steel, our alloy showed similar biocompatibility but with significantly higher antibacterial activity. Our results validated the feasibility of using magnesium alloys to manufacture biodegradable ureteral stents, and improved our knowledge on how the urinary tract responds to the increase of metallic ion concentration and pH.

Acknowledgements

This study was supported by National Natural Science Foundation of China [grant number 51771045] and the Fundamental Research Funds for the Central Universities [grant number N2002016].

We sincerely thank all the staff in Animal Experimental Center, Anesthesia Department, Imaging department and Clinical Laboratory of General Hospital of Northern Theater Command; Prof. Dongwei Xue and Dr. Jia Liu in China Medical University for the surgical operations; Dr. Qian Sun, Dr. He Zhang for their help with the animal experiment; Prof. Himing Qin, Prof. Deliang Zhang, Prof. Tong Cui, Dr. Guosheng Duan, Dr. Xiang Wang and Dr. Yuxiang Wang for their assistance with material characterization and histopathological observation; colleagues in Helmholtz-Zentrum Geesthacht and University of California, Riverside for providing experimental instruments and good guidance.

Statement of Significance

To our knowledge, this is the first *in vivo* study of biodegradable magnesium alloy urinary implants in large animal models. Due to the rheo-solidification process, refined microstructure, higher tensile strength and more homogeneous corrosion rate were achieved. The degradation process was homogenous and perfectly fitted the average clinical indwelling time. Compared with the widely used ureteral stent material, stainless steel, our alloy showed similar biocompatibility but significantly higher antibacterial activity. Our results validated the feasibility of using magnesium alloys for manufacturing biodegradable ureteral stents, and may also contribute to a

better understanding of how the urinary tract responds to increasing metal ion concentration and pH fluctuation.

Declarations of interest: none

Declaration of interests

The authors declare that they have no known competing financial interests or personal relationships that could have appeared to influence the work reported in this paper.

References

[1] C. Forbes, K.B. Scotland, D. Lange, B.H. Chew, Innovations in Ureteral Stent Technology, *Urol. Clin.* 46(2) (2019) 245-255.

[2] A. Roguin, Stent: The Man and Word Behind the Coronary Metal Prosthesis, *Circ. Cardiovasc. Interv.* 4(2) (2011) 206-209.

[3] J.S. Lam, M. Gupta, Ureteral Stents, in: M.L. Stoller, M.V. Meng (Eds.), *Urinary Stone Disease: The Practical Guide to Medical and Surgical Management*, Humana Press, Totowa, NJ, 2007, pp. 465-493.

[4] R.P. Finney, S.C. Hopkins, Ureteric Stents, in: J.P. Pryor (Ed.), *Urological Prostheses, Appliances and Catheters*, Springer London, London, 1992, pp. 33-72.

[5] R.P. Finney, Experience with New Double J Ureteral Catheter Stent, *J. Urol.* 120(6) (1978) 678-681.

- [6] G.M. Sali, H.B. Joshi, Ureteric stents: Overview of current clinical applications and economic implications, *Int. J. Urol.* 27(1) (2020) 7-15.
- [7] S. Sundaramurthy, R. Joseph Thomas, K. Herle, Jeyaseelan, J. Mathai, J. Jacob Kurian, Double J stent removal in paediatric patients by Vellore Catheter Snare technique: a randomised control trial, *J. Pediatr. Urol.* 15(6) (2019) 661.e1-661.e8.
- [8] N. Disma, J.D. O'Leary, A.W. Loepke, A.M. Brambrink, K. Becke, N.G. Clausen, J.C. De Graaff, F. Liu, T.G. Hansen, M.E. McCann, C.F. Salorio, S. Soriano, L.S. Sun, P. Szmuk, D.O. Warner, L. Vutskits, A.J. Davidson, Anesthesia and the developing brain: A way forward for laboratory and clinical research, *Pediatr. Anesth.* 28(9) (2018) 758-763.
- [9] L. Vutskits, A. Davidson, Update on developmental anesthesia neurotoxicity, *Curr. Opin. Anesthesio.* 30(3) (2017) 337-342.
- [10] J.L. Lu, Y.H. Lu, Y. Xun, F. Chen, S.G. Wang, S.Y. Cao, Impact of Endourological procedures with or without double-J stent on sexual function: a systematic review and meta-analysis, *BMC Urol.* 20(1) (2020) 8.
- [11] F. Soria, E. Morcillo, A. Serrano, A. Budia, I. Fernandez, T. Fernandez-Aparicio, F.M. Sanchez-Margallo, Evaluation of a New Design of Antireflux-biodegradable Ureteral Stent in Animal Model, *Urology* 115 (2018) 59-64.
- [12] S. Champagne, E. Mostaed, F. Safizadeh, E. Ghali, M. Vedani, H. Hermawan, In Vitro Degradation of Absorbable Zinc Alloys in Artificial Urine, *Materials* 12(2) (2019) 295.
- [13] C.M. Li, C.C. Guo, V. Fitzpatrick, A. Ibrahim, M.J. Zwierstra, P. Hanna, A. Lechtig, A. Nazarian, S.J. Lin, D.L. Kaplan, Design of biodegradable, implantable devices towards clinical translation, *Nat. Rev. Mater.* 5(1) (2020) 61-81.
- [14] D.W. Zhao, F. Witte, F.Q. Lu, J.L. Wang, J.L. Li, L. Qin, Current status on clinical applications of magnesium-based orthopaedic implants: A review from clinical translational perspective, *Biomaterials* 112 (2017) 287-302.
- [15] A.A. Barros, S. Browne, C. Oliveira, E. Lima, A.R.C. Duarte, K.E. Healy, R.L. Reis, Drug-eluting biodegradable ureteral stent: New approach for urothelial tumors of upper urinary tract cancer, *Int. J. Pharmaceut.* 513(1-2) (2016) 227-237.
- [16] J.Y. Lock, E. Wyatt, S. Upadhyayula, A. Whall, V. Nunez, V.I. Vullev, H. Liu, Degradation and antibacterial properties of magnesium alloys in artificial urine for potential resorbable ureteral stent applications, *J. Biomed. Mater. Res. A* 102(3) (2014) 781-792.
- [17] S. Zhang, Y. Bi, J. Li, Z. Wang, J. Yan, J. Song, H. Sheng, H. Guo, Y. Li, Biodegradation behavior of magnesium and ZK60 alloy in artificial urine and rat models, *Bioact. Mater.* 2(2) (2017) 53-62.
- [18] P. Betschart, V. Zumstein, M.T. Buhmann, S. Altenried, C. Babst, G. Mullhaupt, S. Gusewell, H.-P. Schmid, Q. Ren, D. Abt, Symptoms Associated With Long-term Double-J Ureteral Stenting and Influence of Biofilms, *Urology* 134 (2019) 72-78.

- [19] F. Witte, F. Feyerabend, P. Maier, J. Fischer, M. Stormer, C. Blawert, W. Dietzel, N. Hort, Biodegradable magnesium-hydroxyapatite metal matrix composites, *Biomaterials* 28(13) (2007) 2163-2174.
- [20] P.K. Bowen, E.R. Shearier, S. Zhao, R.J. Guillory, F. Zhao, J. Goldman, J.W. Drelich, Biodegradable Metals for Cardiovascular Stents: from Clinical Concerns to Recent Zn-Alloys, *Adv. Healthcare Mater.* 5(10) (2016) 1121-1140.
- [21] D. Hernandez-Escobar, S. Champagne, H. Yilmazer, B. Dikici, C.J. Boehlert, H. Hermawan, Current status and perspectives of zinc-based absorbable alloys for biomedical applications, *Acta Biomater.* 97 (2019) 1-22.
- [22] T. Jin, Y. He, Antibacterial activities of magnesium oxide (MgO) nanoparticles against foodborne pathogens, *J. Nanopart. Res.* 13(12) (2011) 6877-6885.
- [23] J. Lellouche, E. Kahana, S. Elias, A. Gedanken, E. Banin, Antibiofilm activity of nanosized magnesium fluoride, *Biomaterials* 30(30) (2009) 5969-5978.
- [24] D. Tie, F. Feyerabend, W.D. Muller, R. Schade, K. Liefelth, K.U. Kainer, R. Willumeit, ANTIBACTERIAL BIODEGRADABLE Mg-Ag ALLOYS, *Eur. Cells Mater.* 25 (2013) 284-298.
- [25] D. Tie, R. Guan, H. Liu, A. Cipriano, Y. Liu, Q. Wang, Y. Huang, N. Hort, An in vivo study on the metabolism and osteogenic activity of bioabsorbable Mg–1Sr alloy, *Acta Biomater.* 29 (2016) 455-467.
- [26] Q. Tian, C. Zhang, M. Deo, L. Rivera-Castaneda, N. Masoudipour, R. Guan, H. Liu, Responses of human urothelial cells to magnesium-zinc-strontium alloys and associated insoluble degradation products for urological stent applications, *Mater. Sci. Eng. C* 96 (2019) 248-262.
- [27] B.M. Liu, Y. Liu, L. Wang, C.S. Hou, M.W. An, RNA-seq-based analysis of the hypertrophic scarring with and without pressure therapy in a Bama minipig model, *Sci. Rep.* 8 (2018) 12.
- [28] D. Tie, B. Zhang, L. Yan, R. Guan, Z. Ji, H. Liu, D. Zhang, D. Liu, M. Chen, Rheological Solidification Behavior and Mechanical Properties of AZ91-Sn Alloys, *Crystals* 9(12) (2019) 641.
- [29] M. Hitchcock, Y. Wang, Z. Fan, Secondary solidification behaviour of the Al-Si-Mg alloy prepared by the rheo-diecasting process, *Acta Mater.* 55(5) (2007) 1589-1598.
- [30] Z. Zareian, M. Emamy, M. Malekan, H. Mirzadeh, W.J. Kim, A. Bahmani, Tailoring the mechanical properties of Mg–Zn magnesium alloy by calcium addition and hot extrusion process, *Mater. Sci. Eng. A* 774 (2020) 138929.
- [31] Regulations for the Administration of Affaires Concerning Experimental Animals, in: T.S.S.a.T.C.o. China (Ed.) 2011.
- [32] K.A. Pasyk, C.A. Hassett, Modified hematoxylin and eosin staining method for epoxy-embedded tissue sections, *Pathol. Res. Pract.* 184(6) (1989) 635-638.
- [33] M.R. McGill, THE PAST AND PRESENT OF SERUM AMINOTRANSFERASES AND THE FUTURE OF LIVER INJURY BIOMARKERS, *Excli J.* 15 (2016) 817-828.

- [34] J. Mair, Progress in myocardial damage detection: New biochemical markers for clinicians, *Crit. Rev. Clin. Lab. Sci.* 34(1) (1997) 1-66.
- [35] H.V. Roohk, A.R. Zaidi, D. Patel, Glycated albumin (GA) and inflammation: role of GA as a potential marker of inflammation, *Inflamm. Res.* 67(1) (2018) 21-30.
- [36] A.A. Nayeb-Hashemi, J.B. Clark, The Mg–Sr (Magnesium-Strontium) system, *Bull. APD* 7(2) (1986) 149-156.
- [37] J.M. Jiang, S. Ni, H.G. Yan, Q. Wu, M. Song, New orientations between beta '(2) phase and alpha matrix in a Mg-Zn-Mn alloy processed by high strain rate rolling, *J. Alloy. Compd.* 750 (2018) 465-470.
- [38] M. Knappek, P. Minarik, J. Capeka, R. Kral, J. Kubasek, F. Chmelik, Corrosion of pure magnesium and a WE43 magnesium alloy studied by advanced acoustic emission analysis, *Corros. Sci.* 145 (2018) 10-15.
- [39] H. Pan, K. Pang, F. Cui, F. Ge, C. Man, X. Wang, Z. Cui, Effect of alloyed Sr on the microstructure and corrosion behavior of biodegradable Mg-Zn-Mn alloy in Hanks' solution, *Corros. Sci.* 157 (2019) 420-437.
- [40] M.P. Gomes, I. Costa, N. Pébère, J.L. Rossi, B. Tribollet, V. Vivier, On the corrosion mechanism of Mg investigated by electrochemical impedance spectroscopy, *Electrochim. Acta* 306 (2019) 61-70.
- [41] M.E. Orazem, I. Frateur, B. Tribollet, V. Vivier, S. Marcelin, N. Pébère, A.L. Bunge, E.A. White, D.P. Riemer, M. Musiani, Dielectric Properties of Materials Showing Constant-Phase-Element (CPE) Impedance Response, *J. Electrochem. Soc.* 160(6) (2013) C215-C225.
- [42] C.-Y. Li, C. Yu, R.-C. Zeng, B.-C. Zhang, L.-Y. Cui, J. Wan, Y. Xia, In vitro corrosion resistance of a Ta₂O₅ nanofilm on MAO coated magnesium alloy AZ31 by atomic layer deposition, *Bioact. Mater.* 5(1) (2020) 34-43.
- [43] G. Perumal, A. Chakrabarti, H.S. Grewal, S. Pati, S. Singh, H.S. Arora, Enhanced antibacterial properties and the cellular response of stainless steel through friction stir processing, *Biofouling* 35(2) (2019) 187-203.
- [44] F. Wolf, V. Paefgen, O. Winz, M. Mertens, S. Koch, N. Gross-Weege, A. Morgenroth, A. Rix, H. Schnoering, K. Chalabi, S. Jockenhoevel, T. Lammers, F. Mottaghy, F. Kiessling, P. Mela, MR and PET-CT monitoring of tissue-engineered vascular grafts in the ovine carotid artery, *Biomaterials* 216 (2019).
- [45] I.J. Kouijzer, F.J. Vos, C.P. Bleker-Rovers, W.J. Oyen, Clinical application of FDG-PET/CT in metastatic infections, *Q. J. Nucl. Med. Mol. Imag.* 61(2) (2017) 232-246.
- [46] M. Esmaily, N. Mortazavi, J.-E. Svensson, M. Halvarsson, D. Bengtsson Blücher, A. Jarfors, M. Wessén, L.-G. Johansson, Atmospheric Corrosion of Mg Alloy AZ91D Fabricated by a Semi-Solid Casting Technique: The Influence of Microstructure, *J. Electrochem. Soc.* 162 (2015) C311-C321.
- [47] L. Choudhary, R.K. Singh Raman, J. Hofstetter, P.J. Uggowitzer, In-vitro characterization of stress corrosion cracking of aluminium-free magnesium alloys for temporary bio-implant applications, *Mater. Sci. Eng. C* 42 (2014) 629-636.

- [48] J. Wang, V. Giridharan, V. Shanov, Z.G. Xu, B. Collins, L. White, Y. Jang, J. Sankar, N. Huang, Y. Yun, Flow-induced corrosion behavior of absorbable magnesium-based stents, *Acta Biomater.* 10(12) (2014) 5213-5223.
- [49] S. Mathieu, C. Rapin, J. Hazan, P. Steinmetz, Corrosion behaviour of high pressure die-cast and semi-solid cast AZ91D alloys, *Corros. Sci.* 44(12) (2002) 2737-2756.
- [50] S. Ardizzone, C.L. Bianchi, M. Fadoni, B. Vercelli, Magnesium salts and oxide: an XPS overview, *Appl. Surf. Sci.* 119(3) (1997) 253-259.
- [51] S. D'Ercole, S. Tete, G. Catamo, G. Sammartino, B. Femminella, D. Tripodi, G. Spoto, M. Paolantonio, MICROBIOLOGICAL AND BIOCHEMICAL EFFECTIVENESS OF AN ANTISEPTIC GEL ON THE BACTERIAL CONTAMINATION OF THE INNER SPACE OF DENTAL IMPLANTS: A 3-MONTH HUMAN LONGITUDINAL STUDY, *Int. J. Immunopathol. Pharmacol.* 22(4) (2009) 1019-1026.
- [52] K. Jurica, V. Benkovic, S. Sikiric, N. Kopjar, I.B. Karaconji, Liver function and DNA integrity in hepatocytes of rats evaluated after treatments with strawberry tree (*Arbutus unedo* L.) water leaf extract and arbutin, *Drug Chem. Toxicol.* 43(2) (2020) 127-137.
- [53] L. Wendt, J. Vider, L.E.S. Hoe, E. Du Toit, J.N. Peart, J.P. Headrick, Complex Effects of Putative DRP-1 Inhibitors on Stress Responses in Mouse Heart and Rat Cardiomyoblasts, *J. Pharmacol. Exp. Ther.* 372(1) (2020) 95-106.
- [54] R.C. Starling, N. Moazami, S.C. Silvestry, G. Ewald, J.G. Rogers, C.A. Milano, J.E. Rame, M.A. Acker, E.H. Blackstone, J. Ehrlinger, L. Thuita, M.M. Mountis, E.G. Soltesz, B.W. Lytle, N.G. Smedira, Unexpected Abrupt Increase in Left Ventricular Assist Device Thrombosis, *N. Engl. J. Med.* 370(1) (2014) 33-40.
- [55] N.R. Sproston, J.J. Ashworth, Role of C-Reactive Protein at Sites of Inflammation and Infection, *Front. Immunol.* 9 (2018) 11.
- [56] A. Kanai, W. de Groat, L. Birder, T. Chai, S. Hultgren, C. Fowler, C. Fry, Symposium report on urothelial dysfunction: Pathophysiology and novel therapies, *J. Urol.* 175(5) (2006) 1624-1629.
- [57] S. Aharony, M. Przydacz, O.L. Van Ba, J. Corcos, Does asymptomatic bacteriuria increase the risk of adverse events or modify the efficacy of intradetrusor onabotulinumtoxinA injections?, *Neurourol. Urodyn.* 39(1) (2020) 203-210.
- [58] Q. Peng, Y. Sun, B. Ge, H. Fu, Q. Zu, X. Tang, J. Huang, Interactive contraction nanotwins-stacking faults strengthening mechanism of Mg alloys, *Acta Mater.* 169 (2019) 36-44.
- [59] D. Yahav, H. Green, N. Eliakim-Raz, E. Mor, S. Husain, Early double J stent removal in renal transplant patients to prevent urinary tract infection - systematic review and meta-analysis of randomized controlled trials, *Eur. J. Clin. Microbiol.* 37(4) (2018) 773-778.
- [60] H. Pelling, J. Nzakizwanayo, S. Milo, E.L. Denham, W.M. MacFarlane, L.J. Bock, J.M. Sutton, B.V. Jones, Bacterial biofilm formation on indwelling urethral catheters, *Lett. Appl. Microbiol.* 68(4) (2019) 277-293.

- [61] K.B. Scotland, J. Lo, T. Grgic, D. Lange, Ureteral stent-associated infection and sepsis: pathogenesis and prevention: a review, *Biofouling* 35(1) (2019) 117-127.
- [62] J.W. Costerton, P.S. Stewart, E.P. Greenberg, Bacterial biofilms: A common cause of persistent infections, *Science* 284(5418) (1999) 1318-1322.
- [63] E.O. Kehinde, V.O. Rotimi, K.A. Al-Awadi, H. Abdul-Halim, F. Boland, A. Al-Hunayan, A. Pazhoor, Factors predisposing to urinary tract infection after J ureteral stent insertion, *J. Urol.* 167(3) (2002) 1334-1337.
- [64] N.-Y.T. Nguyen, N. Grelling, C.L. Wetteland, R. Rosario, H. Liu, Antimicrobial Activities and Mechanisms of Magnesium Oxide Nanoparticles (nMgO) against Pathogenic Bacteria, Yeasts, and Biofilms, *Sci. Rep.* 8(1) (2018) 16260.
- [65] D.A. Robinson, R.W. Griffith, D. Shechtman, R.B. Evans, M.G. Conzemius, In vitro antibacterial properties of magnesium metal against *Escherichia coli*, *Pseudomonas aeruginosa* and *Staphylococcus aureus*, *Acta Biomater.* 6(5) (2010) 1869-1877.
- [66] C. Dong, J. Cairney, Q. Sun, O.L. Maddan, G. He, Y. Deng, Investigation of Mg(OH)₂ nanoparticles as an antibacterial agent, *J. Nanopart. Res.* 12(6) (2010) 2101-2109.
- [67] F. Friedersdorff, S. Weinberger, N. Biernath, H. Plage, H. Cash, N. El-Bandar, The Ureter in the Kidney Transplant Setting: Ureteroneocystostomy Surgical Options, Double-J Stent Considerations and Management of Related Complications, *Curr. Urol. Rep.* 21(1) (2020) 5.
- [68] A. Breda, M.H. Bui, J.C. Liao, H.A. Gritsch, P.G. Schulam, Incidence of ureteral strictures after laparoscopic donor nephrectomy, *J. Urol.* 176(3) (2006) 1065-1068.
- [69] L. Baumgarten, A. Desai, S. Shipman, D.D. Eun, M.A. Pontari, J.H. Mydlo, A.C. Reese, Spontaneous passage of ureteral stones in patients with indwelling ureteral stents, *Can. J. Urol.* 24(5) (2017) 9024-9029.
- [70] J.M. Kuebker, J. Robles, J.J. Kramer, N.L. Miller, S.D. Herrell, R.S. Hsi, Predictors of spontaneous ureteral stone passage in the presence of an indwelling ureteral stent, *Urolithiasis* 47(4) (2019) 395-400.
- [71] K.H. Bichler, E. Eipper, K. Naper, Infection-induced urinary stones, *Urologe A* 42(1) (2003) 47-+.
- [72] J.J. Sigurdarson, S. Svane, H. Karring, The molecular processes of urea hydrolysis in relation to ammonia emissions from agriculture, *Reviews in Environmental Science and Bio/Technology* 17(2) (2018) 241-258.
- [73] K. Brust, A. Evans, R. Plemmons, Favourable outcome in the treatment of carbapenem-resistant Enterobacteriaceae urinary tract infection with high-dose tigecycline, *J. Antimicrob. Chemoth.* 69(10) (2014) 2875-2876.
- [74] Z. Ma, M. Gao, D. Na, Y. Li, L. Tan, K. Yang, Study on a biodegradable antibacterial Fe-Mn-C-Cu alloy as urinary implant material, *Mater. Sci. Eng. C* 103 (2019) 109718.
- [75] Y.A. Qing, K.S. Li, D.D. Li, Y.G. Qin, Antibacterial effects of silver incorporated zeolite coatings on 3D printed porous stainless steels, *Mater. Sci. Eng. C* 108 (2020) 5.

[76] I. Burghardt, F. Luethen, C. Prinz, B. Kreikemeyer, C. Zietz, H.-G. Neumann, J. Rychly, A dual function of copper in designing regenerative implants, *Biomaterials* 44 (2015) 36-44.

Figure captions

Fig. 1. Study design and material characterization. (a) Schematic representation of the fabrication process and dimensions of the stent, the animal model and the surgical procedure. (b) Optical microstructure of the semisolid rheo-formed ZJ41 alloy. (c) SEM microstructure of ZJ41 alloy with EDS analysis results. (d) EDS mapping of ZJ41 alloy. (e) XRD pattern of ZJ41 alloy. (f) HR-TEM micrograph of the alloy showing the boundary between primary solid phase and secondary grain phase and the corresponding electron diffraction pattern.

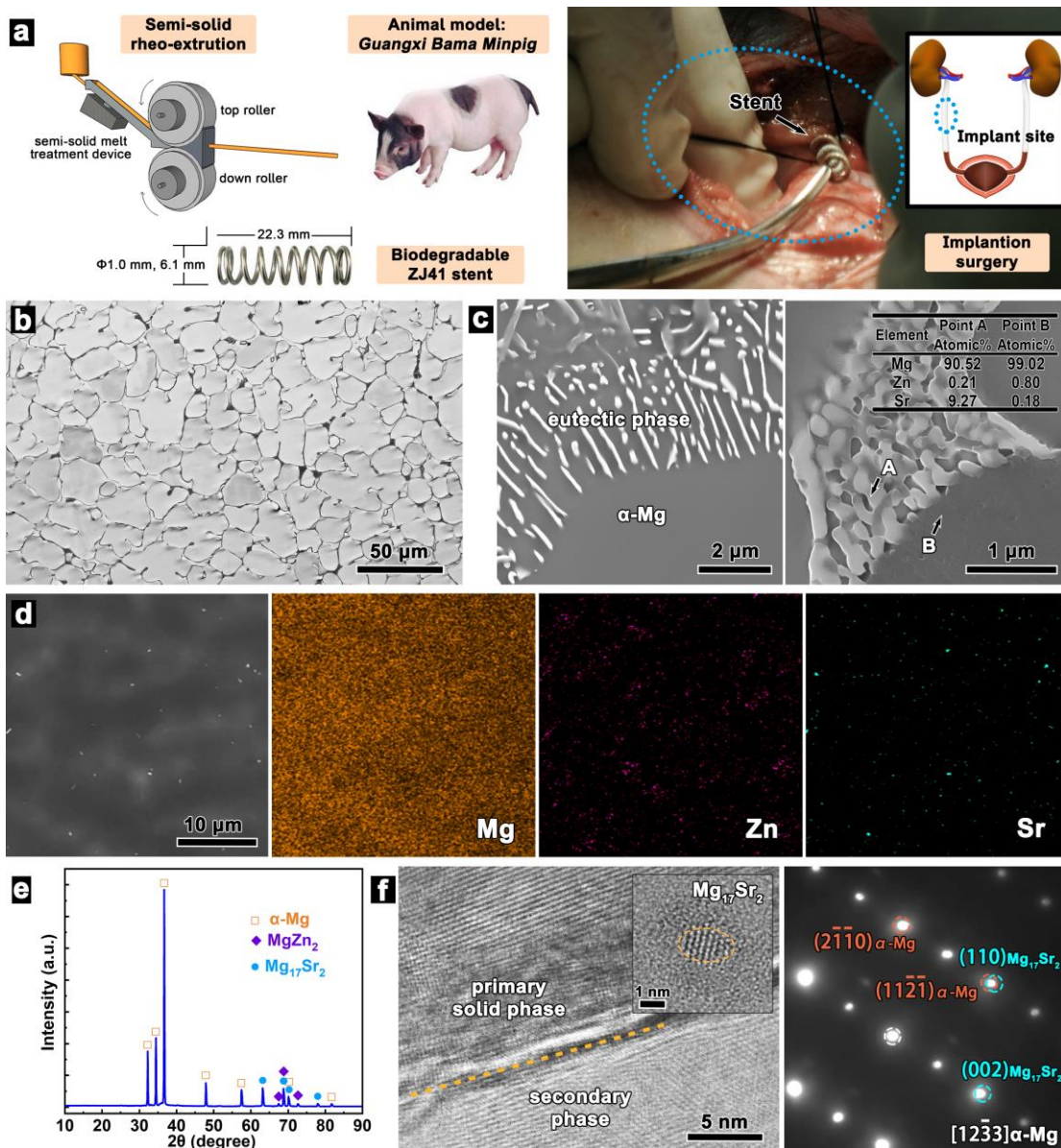


Fig. 2. Electrochemical results and cytocompatibility. (a) Polarization curves of ZJ41 alloy measured in AU. (b) Cyclic voltammetry curves of ZJ41 alloy in logarithmic scale measured in AU. (c) Nyquist diagram of ZJ41 alloy in AU at OCP with its equivalent circuit, where R_1 stands for the solution resistance; R_2 stands for the film resistance pore resistance; R_3 stands for the charge transfer resistance; CPE_1 corresponds to the constant phase angle element of the corrosion product film; CPE_2 corresponds to the double layer capacitance. (d) The changes of corrosion rate and pH value in AU as a function of immersion time. (e) Fluorescent microscope images and CCK-8 proliferation rate of LO2 cells after 7, 14, and 21 days incubation on SS and ZJ41 alloy, where living cells were stained green while dead cells were stained red (scale bars, 50 μ m).

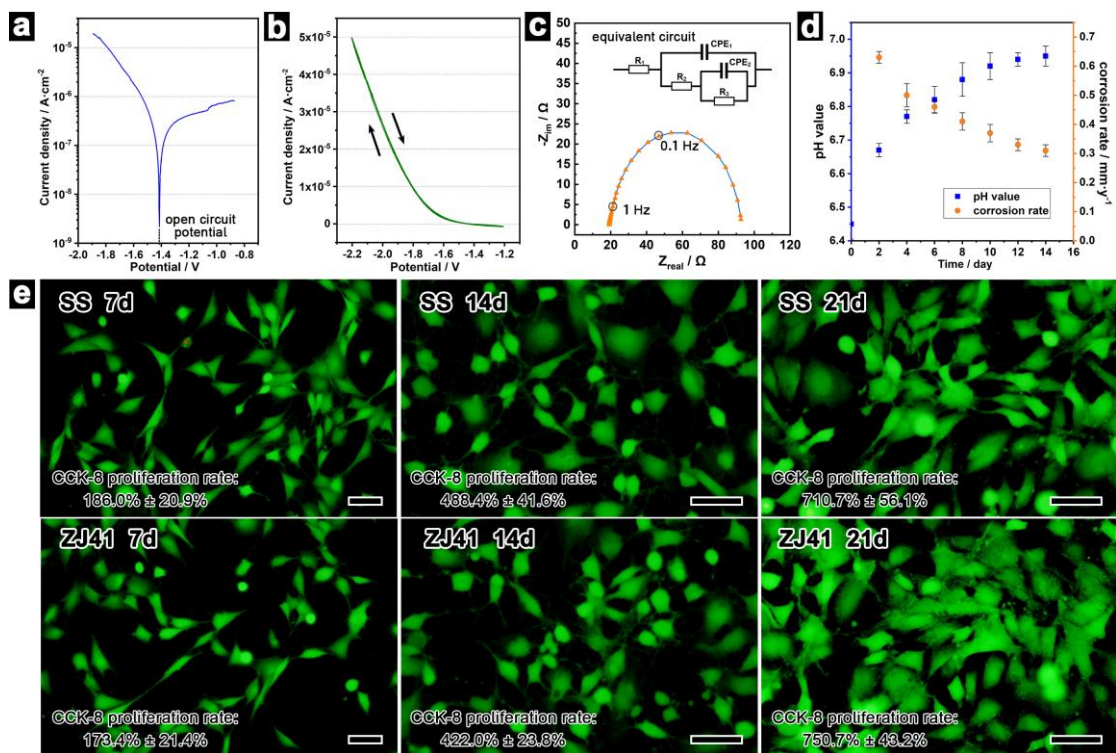


Fig. 3. *In vivo* degradation. (a) PET- CT images 0, 7, 14 weeks after ZJ41 implantation into the animals; the framed areas indicate the implantation site. (b) The changes of total urine magnesium content and the calculated residual mass of the ZJ41 stents as a function of time. (c) The surface SEM morphology of the ZJ41 stent after 7 weeks implantation, where the circled areas correspond to the primary solid phases of the ZJ41 alloy. (d) Mg 2p XPS spectra for the surface layer of ZJ41 alloy after 7 weeks implantation.

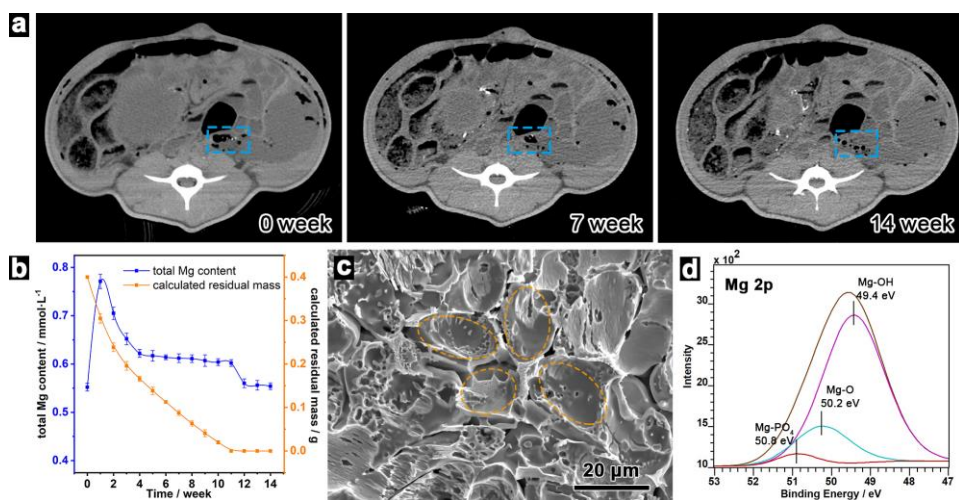


Fig. 4. Histocompatibility and key biological indices. (a) Representative H/E stained liver sections at 14 weeks post-implantation (scale bars, 100 μm). (b) Main hepatic function indexes of the test animals during the implantation period. (c) Representative H/E stained myocardium sections at 14 weeks post-implantation (scale bars, 50 μm). (d) Main cardiac function markers of the test animals

during the implantation period. (e) Hematological serum indices at 0, 7, and 14 weeks post-implantation. Results are displayed as mean value \pm SD. Significant differences are marked with * ($p < 0.05$), ** ($p < 0.01$) and *** ($p < 0.001$), and NS stands for no significant difference.

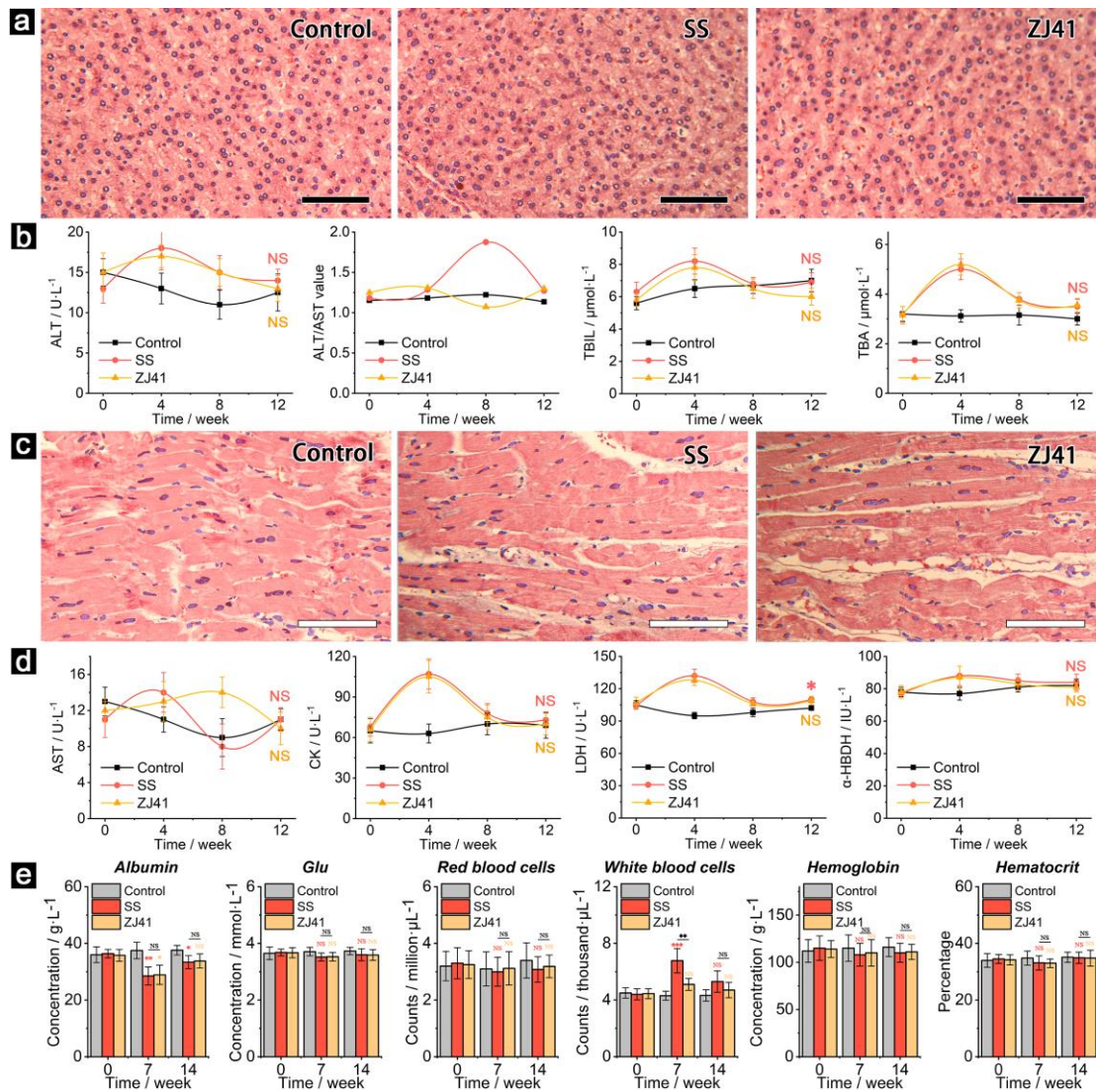
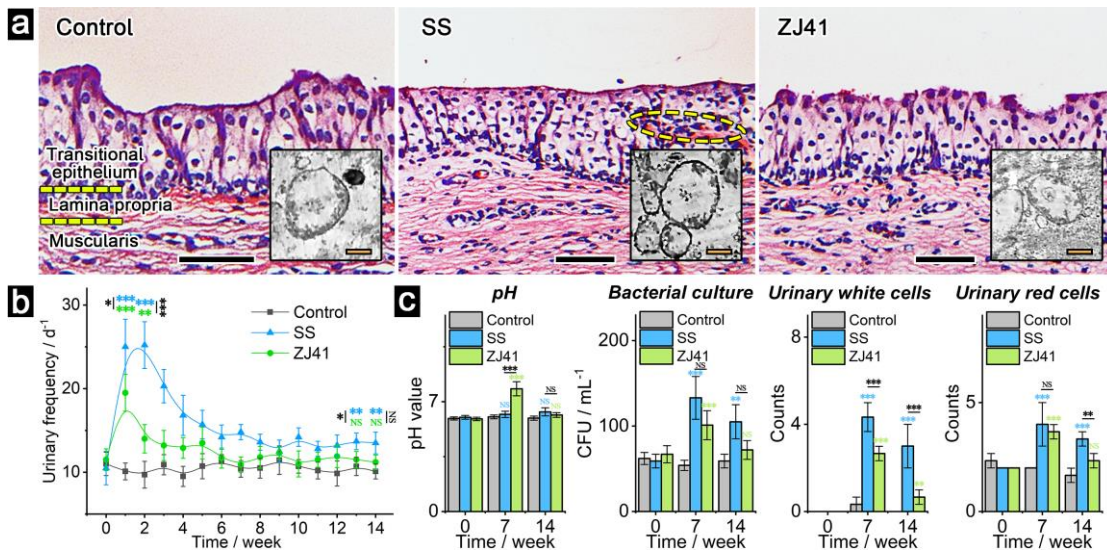


Fig. 5. Impact of the stents on lower urinary tract. (a) Representative ureteral wall tissues at 14 weeks post-implantation (scale bars, 100μm) with cellular morphology by TEM observation in higher resolution (scale bars, 5μm); the circled area in the SS group indicates calcification toward the luminal aspect of the ureter wall with peri-implant infection present. (b) The changes of urinary frequency of the test animals during the implantation period. (c) Urinalysis results of the test animals at 0-, 7- and 14 weeks post-implantation. The results were presented in mean value (six duplicates) \pm SD. Significant differences are labeled with * ($P < 0.05$), ** ($P < 0.01$) and *** ($P < 0.001$); NS stands for no significant difference.



Graphical abstract

